Clays and Clay Minerals, Vol. 66, No. 2, 190–207, 2018.

MINERALOGY AND GEOCHEMISTRY OF LIMONITE AS A WEATHERING PRODUCT OF ILVAITE IN THE YESHAN IRON DEPOSIT, TONGLING, CHINA

PING CHEN, TIANHU CHEN*, QIAOQIN XIE, LIANG XU, HAIBO LIU, AND YUEFEI ZHOU

Laboratory for Nanomineralogy and Environmental Material, School of Resources and Environmental Engineering, Hefei University of Technology, 230009, China

Abstract—Limonite is mainly derived from weathering of Fe sulfide, iron-bearing carbonate, or silicate minerals. The weathering of Fe sulfide or carbonate minerals to yield limonite from the Tongling mineralization cluster has been studied extensively. Knowledge of the mineralogical and geochemical characteristics of the limonite from weathering of Fe-bearing silicate minerals is still incomplete, however. To address this, black limonite containing ilvaite (a silicate mineral) found in Yeshan iron deposit, Tongling, China, was studied using mineralogical and chemical analysis. The mineralogical characteristics indicated that Mn goethite was present as nano-granular (<15 nm) or acicular (50−100 nm long, ~10 nm wide, *i.e.* high length/width ratio) crystals with low crystallinity. Groutite, ramsdellite, and pyrolusite were identified in the limonite as ~5 nm nanoparticles, and coated on the goethite surface. Amorphous Fe-Mn phases and silica were highly developed in the limonite studied. Ilvaite crystals showed idiomorphic granular morphology and were replaced by Fe-Mn oxides/hydroxides; pyrite was also present as inclusions within the ilvaite and the ilvaite structural formula calculated was $Ca_{1.04}(Fe_{1.57}Mn_{0.31}Mg_{0.04})(Fe_{1.09}Al_{0.01})[Si_{1.95}O]O(OH)$. According to the relatively high CuO and ZnO values and the low Al_2O_3 value in the black limonite, the negative correlations between (Fe_2O_3+MnO) and (CuO+ZnO+BaO), (Fe_2O_3+MnO) and Al_2O_3, high Mn and Si contents, and the characteristics of the textural relationships and compositions between the black limonite and ilvaite, a semi-enclosed environment with acidic to weakly alkaline conditions was deduced; ilvaite was found to be responsible for the formation and enrichment of limonite.

Key Words—Geochemistry, Limonite, Mn-bearing Ilvaite, Nanomineralogy, Tongling, Weathering.

INTRODUCTION

Limonite, a mineral aggregate, consisting mainly of ferric (oxyhydr)oxides including goethite and ferrihydrite, is an important source of iron ore and is distributed widely in supergene environments. Over recent decades, limonite has been studied widely for its mineralogy (Nambu *et al*., 1955; Kelly, 1957; Okada *et al*., 1966), geochemistry (Abe, 1972; Bustamante *et al*., 2005), genesis or mechanism of formation (Stone *et al*., 1934; Blanchard and Boswell *et al*., 1935; Vaasjoki, 1985), mineral processing (Song *et al*., 2002; O'Connor *et al*., 2006; Tang and Valix, 2006; Wu *et al*., 2017), and for possible applications (Kaneko *et al*., 2002; Li, L. *et al*., 2007; Tsubouchi *et al*., 2017; Zhao *et al*., 2017). Studies of mineral deposits and some simulations in the laboratory have indicated that limonite is the weathering product of Fe-sulfide minerals, Fe-carbonate minerals, and Fe-enriched silicate minerals. Geological, microbiological, and environmental contexts are all considered here, *e.g.* the Fe-sulfide minerals weathered to limonite are also referred to as 'gossan' and this is an important carrier of gold (Bowell, 2010; Velasco *et al*., 2013; Andreu *et al*., 2015; Yesares *et al*., 2015, 2017). Fe carbonate weathered to limonite may greatly affect the global carbon cycle (Frisbee and Hossner, 1995). The Fe-enriched silicate minerals (such as olivine) weathered to limonite play an important role in the formation of soil (Williams *et al*., 2012), as confirmed by Fe-speciation and isotope-fractionation studies during silicate weathering and soil formation (Kiczka *et al*., 2011); microorganisms can also have a significant effect on the process of weathering of silicate minerals such as garnet (Embrechts and Stoops, 1982).

Limonite is also distributed widely in the middle−lower Yangtze valley metallogenic belt in southeast China. Previous research has focused mainly on the genesis of gossan gold deposits, the regularity of their occurrences, and the evaluation of the resources (Li, 1980; Liu, 1989; Sheng and Wang, 1989; He *et al*., 1992; Li *et al*., 1992; Yao *et al*., 1992; Sun and Chu, 2006; Cai, 2006). Studies have indicated that in the shallow surface of the Tongling mineralization cluster, particularly in the Xinqiao, Daijiahui, Niushan, Huangshilao, Jiguanshan, Bailing, and Taoyuan areas, most limonite is a weathering product of Fe-sulfide or carbonate minerals (Cao and Kong, 1991; Liu, 2016). Fe-sulfide minerals or siderite weathered to limonite from the Xinqiao area

* E-mail address of corresponding author:
chentianhu@hfut.edu.cn
DOI: 10.1346/CCMN.2018.064102

This paper was originally presented during the 3rd Asian Clay Conference, November 2016, in Guangzhou, China

have been found to differ greatly in terms of their chemical composition, mineralogy, and micromorphology (Liu, 2016). Little information about the Fe-enriched silicate minerals weathered to limonite in the Tongling mineralization cluster is available, especially in terms of the mineralogical and geochemical characteristics.

The discovery of well developed limonite in the Yeshan iron deposit, Tongling, has led to significant interest. Field investigations have revealed that its peculiar texture and structure are very different from limonite at other locations, and the main associated gangue mineral is ilvaite. Ilvaite is a typical skarn mineral and commonly occurs in skarn iron deposits or copper-zinc-iron polymetallic skarn deposits as a product of retrograde alteration in the early skarn stage (Naslund *et al.*, 1983; Agata and Adachi, 1995; Franchini, 2002; Bonev *et al.*, 2005; Endo, 2017). Like other silicate minerals such as pyroxene and feldspar, ilvaite is unstable at ambient conditions; mineralogical and geochemical studies of limonite from ilvatite will improve understanding of the nanogeochemical processes of weathering of Fe-enriched silicate.

The main objective of the present study was to investigate the mineralogical and geochemical characteristics of limonite in the Yeshan iron deposit and relationships between the limonite and ilvaite. This may provide some new information about the physicochemical conditions of the limonite weathering process and may also be helpful in differentiating skarn-weathered limonite from other types and to guide exploration of similar limonite deposits elsewhere. Furthermore, such insights may also be important for further understanding the geochemical processes of weathering of silicate minerals in supergene environments.

GEOLOGICAL SETTING

The Yeshan iron deposit is located southwest of Zhongming town in Tongling, Anhui Province, China (Figure 1). Tectonically, it is located on the northwest limb of the Shu Jiadian anticline, on the north rim of the Tongling uplift (Xu *et al*., 2011).

The stratigraphy of the study area spans the Upper Devonian Wutong Formation, the Middle Carboniferous Huanglong Formation, the Upper Carboniferous Chuanshan Formation, the Lower Permian Qixia Formation, and Quaternary sediments. The lower Wutong Formation comprises gravel-bearing quartz sandstone, quartz sandstone interbedded with siltstone, silty shale, and shale; fine sandy siltstone, siltstone, pelitic siltstone, and silty shale interbedded with quartz sandstone make up the upper part of the formation. The Carboniferous Huanglong Formation is dominated by dolomite and bioclastic limestone. The Wutong and Huanglong formations are missing from some parts of the study area due to a longitudinal thrust, which marks the upper boundary of the Wutong Formation. Bioclastic limestone and pelletized limestone appear in the Chuanshan Formation. The lower Qixia Formation is dominated by bioclastic limestone with silty shale and carbonaceous sandshale, and the upper Qixia Formation consists of bioclastic limestone, chert-bearing limestone and banded limestone. Magmatic rocks in the ore district include granodiorite porphyry, quartz monzonitic porphyrite, and pyroxene monzodiorite, with granodiorite and diorite porphyry being related to this particular deposit.

Five orebodies trending from northwest to southeast in the Yeshan iron deposit are 70–300 m long and 5–50 m wide and are stratiform or stratoid. Four of the ore bodies (numbers I, II, IV, and V) are hosted within the Huangong and Huanglong/Chuanshan Formations, while one (number III) is hosted in the upper Wutong Formation. The strike of the orebodies is parallel to that of the host strata. The alteration of the wall rock is weak; mostly silicification and sericitization, with only partial pyritization. Skarnization and marmarization are weakly developed in the contact zone. The metallic minerals include specularite, goethite, minor hematite, magnetite, and pyrite. The main gangue mineral is quartz; some ilvaite appears in the deeper parts of the ore body. Limonitization is common throughout the five ore bodies, and the maximum reserves are located in the number V ore body, which lies above the specularite orebody (Figure 2a).

SAMPLING AND EXPERIMENTAL METHODS

Sampling

Limonite samples selected from the number V ore body of the Yeshan iron deposit (Figures 1, 2a, 2b) were divided into three groups according to the color, texture, and structure of the ore: (1) loose, black, radial limonite (Figure 2c,d); (2) loose, brown limonite (Figure 2c,d); and (3) dense, black, massive limonite (Figure 2e). The loose, black, radial limonite comprises 65% of all the limonite, while the loose, brown limonite accounted for no more than 5%. Microscopically, goethite in the dense, black, massive limonite showed a granular texture. Fractures were filled with hematite and quartz (Figure 3a,b). Ilvaite was replaced by goethite at the contact of the two minerals, indicating that ilvaite was the main original mineral in the formation of limonite during weathering. Ilvaite was idiomorphic and coarse in size, containing parcels of pyrite and with veins filled with hematite or quartz (Figure 3c,d).

Experimental methods

Fresh limonite ores obtained from the field were washed with deionized water and dried at 70ºC in the oven for 5 h. Then, the three kinds of limonite samples were separated by crushing (by means of hammering) into small fragments (~0.5 mm in size) (the loose, brown limonite was handled with extra care) and then sieved

https://doi.org/10.1346/CCMN.2018.064102a Published online by Cambridge University Press

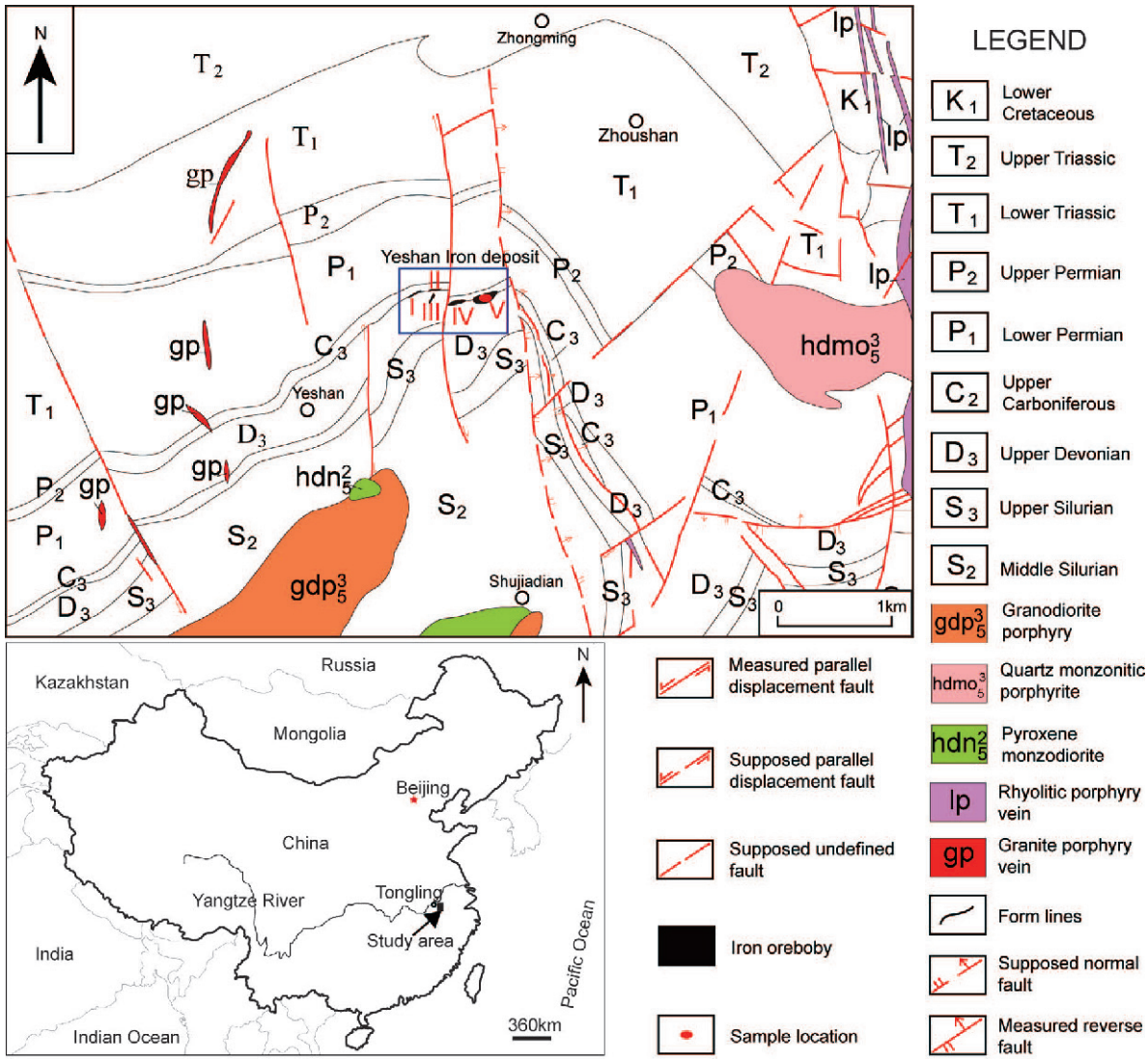

Figure 1. Simplified geological map of the Yeshan iron deposit, Tongling (modified after map No. 321 of the Bureau of Geology and Mineral Exploration of Anhui Province, 1989).

through a standard 200 mesh (75 μm) sieve after further grinding by hand for several minutes using an agate mortar. These powders were used for X-ray diffraction (XRD), X-ray fluorescence (XRF), and thermogravimetric (TG) analyses at the Analysis and Testing Center of Hefei University of Technology, China.

The XRD measurements were performed using a Rigaku powder diffractometer (D/MAX 2500V PC, Tokyo, Japan) with CuKα radiation. The tube voltage was 40 kV and the current was 30 mA, the scan rate was 1.2º2θ min^{-1} with 0.5º2θ divergence slit size. A Shimadzu XRF-1800 (Shimadzu Corp., Kyoto, Japan) with Rh radiation was chosen to measure the chemical composition. A Netzsch STA449C instrument (Netzsch Co., Selb, Germany) was used for TG analysis; ~20 mg of finely powdered samples was heated in an open corundum crucible from 25 to 800ºC at a heating rate of 5ºC/min under a flowing N_2 atmosphere (20 mL/min).

Representative limonite samples were prepared for field-emission scanning electron microscopy (FE-SEM) analysis by sticking the fresh, broken particles onto an aluminum stub with double-sided tape and coating thinly with gold by spraying for 120 s. The FE-SEM images were obtained using a JSM-6700LV (JEOL Ltd, Tokyo, Japan) scanning electron microscope equipped with an energy dispersive spectrometer (EDS). The limonite particles for transmission electron microscopy (TEM) analysis were dispersed in an ultrasonic ethanol bath for ~30 min and one drop of each suspension was placed on a Cu grid. The TEM images were collected using a JEM-2100 (JEOL Ltd, Tokyo, Japan) coupled with an energy dispersive spectrometer (EDS), and operated at 200 keV.

https://doi.org/10.1346/CCMN.2018.064102a Published online by Cambridge University Press

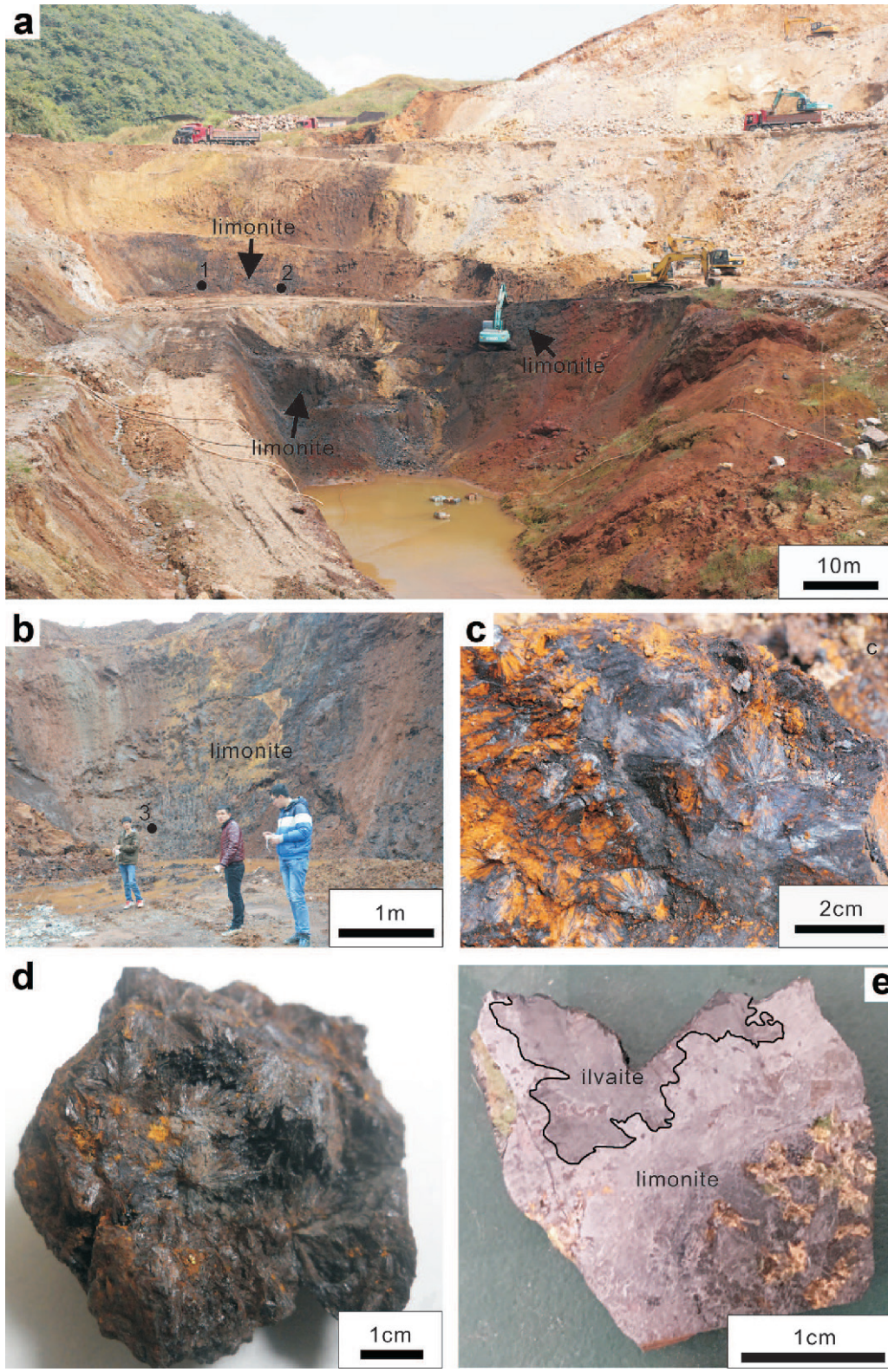

Figure 2. Photographs of the stope and representative samples: (a) first geological investigation of a mine; (b) second geological investigation of a mine, its location is equivalent to numbers 1 and 2 in part a; (c, d e) samples from sampling points 1, 2, and 3, respectively.

https://doi.org/10.1346/CCMN.2018.064102a Published online by Cambridge University Press

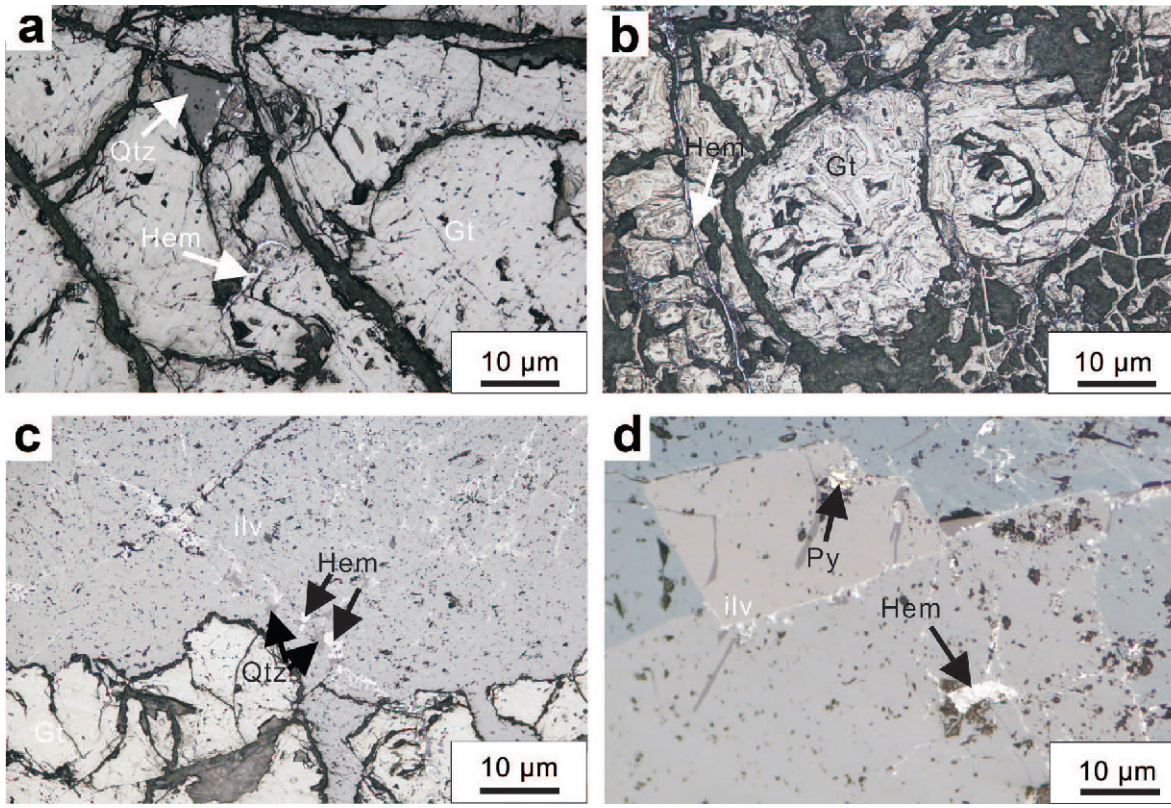

Figure 3. Photomicrographs of the dense, massive limonite: (a,b) goethite shows an allotriomorphic granular texture; some hematite and quartz filled in or distributed along a fracture in goethite; (c) hematite fills in ilvaite as a vein with quartz, and ilvaite replaced by goethite; (d) pyrite encircled by ilvaite or hematite fills in the ilvaite. Gt – goethite, Qtz – quartz, Hem – hematite, Ilv – ilvaite, Py – pyrite.

The FE-SEM and TEM were carried out in the Analysis and Testing Center of Hefei University of Technology, China.

In order to estimate the Mn oxides content, amorphous Fe-Mn phases, amorphous silica, and various kinds of limonite (0.2 g) were treated with 200 mL of 0.1 M hydroxylamine hydrochloride solution (Tang, 2000; Neaman *et al*., 2004), then with 200 mL of 0.2 M oxalic acid/0.2 M ammonium oxalate solution (Alvarez *et al*., 2005), and finally with 200 mL of 0.1 M hydroxylamine hydrochloride solution, of which solvent was 20% hydrochloric acid. The first two treatments were carried out at room temperature and shaken in the dark for 2 h, while the third treatment was performed at 60ºC in the water bath and shaken for 12 h. After that, suspensions were centrifuged, dried, and weighed, while some were mixed with alcohol before deposition on a Cu grid for TEM observation (if necessary). All chemicals (Sinopharm Chemical Reagent Co., Ltd, Shanghai, China) were of analytical grade, all solutions were prepared in deionized water, and all experiments were repeated three times.

Major-element concentrations in ilvaite (trace elements were not discussed here), were measured using laser ablation-inductively coupled plasma-mass spectrometry (LA-ICP-MS) on polished thick thin-sections, using an Agilent 7900 Quadrupole ICP-MS (Agilent Technologies Inc., Santa Clara, California, USA) coupled to an Analyte HE 193-nm ArF Excimer Laser Ablation system (Photon Machines Inc., Bozeman, Montana, USA). A squid signal smoothing device is included in this laser ablation system. Each analysis was performed on a uniform spot-size diameter of 35 μm at 6 Hz with energy of ~6–10 mJ/cm^2 for 40 s after measuring the gas blank for 20 s. Standard reference materials, such as the USGS synthetic basalt glasses, GSE-1G and GSC-1G, and the USGS basalt glass, BCR-2G, were used as external standards to plot calibration curves; GSE-1G was used as a quality control to correct time-dependent signal drift and mass discrimination. The preferred values of element concentrations for the USGS reference glasses are from the GeoReM database (http://georem.mpch-mainz.gwdg.de/). After every 15 sample analyses, analyses of standard reference materials were carried out, and standards were run again after each 15 unknowns. Detection limits were calculated for each element in each spot analysis. The off-line data processing was performed using the program

https://doi.org/10.1346/CCMN.2018.064102a Published online by Cambridge University Press

ICPMSDataCal (Liu, 2010; Liu *et al*., 2008, 2010). The sum of all element concentrations expressed as oxides (according to their oxidation states in ilvaite) were considered to be 100 wt.% for a given anhydrous silicate mineral. The analytical error for major elements in minerals was 5%.

RESULTS

XRD

The XRD patterns for the different limonites showed no distinct differences among the black massive (Figure 4a), black radial (Figure 4b), and brown limonites (Figure 4c). Goethite was the most abundant weathering product in these limonites; all goethites showed weak, wide, and dispersed diffraction peaks (110, 130, 111), indicating that they had low crystallinity. A weak peak at 26.64º2θ (3.34 Å) was due to a small amount of quartz in the black limonite. In the dense, black, massive limonite (Figure 4d), hematite was identified from diffraction peaks at 2.71 Å and 2.52 Å, while ilvaite was also detected, based on the characteristic diffraction peaks at 7.31, 2.87, 2.84, 2.71, and 2.68 Å.

XRF and LA-ICP-MS

The chemical compositions (Table 1) of the black limonite (no related data are given for the loose, brown limonite because of its random distribution and small amount) show that the massive limonite consisted of Fe_2O_3 72.63–77.39 wt.%, MnO 6.19–8.48 wt.%, SiO_2 3.75–4.35 wt.%, and loss on ignition (LOI) ~12 wt.%. The radial limonite showed a similar composition with Fe_2O_3 57.93–58.74 wt.%, MnO 14.62–17.50 wt.%, Al_2O_3 0.79–2.09 wt.%, SiO_2 4.01–6.13 wt.%, and ZnO 0.43–4.05 wt.% (LOI ~15 wt.%). No distinct differences between the two were found, but the Fe content was greater in the dense, black massive limonite, while values for Al, Mn, Zn, Ca, Cu, and Ba were less. The LOI values for these two are different but both are greater than the theoretical value for goethite (Frost *et al*., 2003). The major elements of ilvaite (Table 2) showed that it was rich in Mn, with MnO 4.24–6.69 wt.%, as well as FeO* (the total amount of Fe) 46.91–49.38 wt.%, SiO_2 29.26–30.02 wt.%, and CaO 14.34–15.08 wt.%. The structural formula of ilvaite yielded on average was, therefore: $Ca_{1.04}(Fe_{1.57}Mn_{0.31}Mg_{0.04})(Fe_{1.09}Al_{0.01})[Si_{1.95}O]O(OH)$.

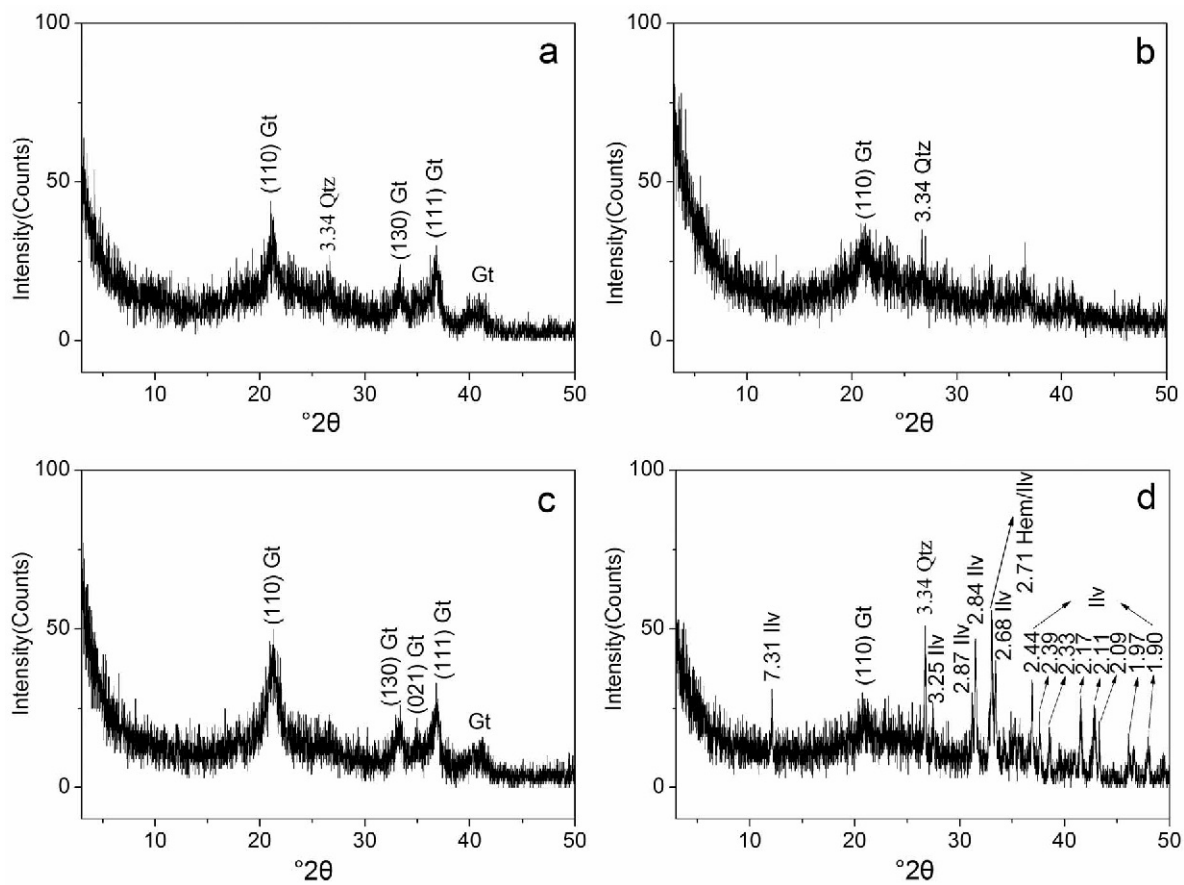

Figure 4. XRD patterns of limonite: (a) dense, black, massive limonite; (b) loose, black, radial limonite; (c) loose, brown limonite; (d) residual ilvaite and hematite in dense, black, massive limonite.

https://doi.org/10.1346/CCMN.2018.064102a Published online by Cambridge University Press

Table 1. XRF analysis results (wt.%) of black limonite from the Yeshan iron deposit.

Samples		SiO_2	Al_2O_3	Fe_2O_3	MnO	CaO	CuO	ZnO	BaO	LOI	Total
Dense, black, massive limonite	YS-1	4.35	0.70	72.63	8.48	0.02	0.17	0.92	bdl	12.55	99.81
	YS-2	4.08	0.56	75.84	6.98	0.02	0.11	0.32		12.05	99.95
	YS-3	3.75	0.24	77.39	6.19	0.02	0.06	0.24		12.04	99.94
	YS-4	4.50	0.70	72.24	8.53	0.02	0.16	0.99		12.65	99.79
Loose, black, radial limonite	YS-5	5.36	0.79	58.58	14.62	0.29	0.03	4.05	0.43	15.61	99.75
	YS-6	5.41	2.71	54.33	15.92	0.02	0.22	1.80	0.23	19.12	99.76
	YS-7	3.91	0.90	63.10	12.88	0.03	1.50	0.59	0.14	16.79	99.85
	YS-8*	6.13	1.98	57.93	16.37	0.13	0.13	1.80	0.32	14.91	99.68
	YS-9*	4.01	2.09	58.74	17.50	0.05	1.11	0.43	0.13	15.73	99.79

Notes: bdl = below detection limit. * from Chen *et al.* (2017)

Thermogravimetric analysis

Thermogravimetric (TG) analysis results for the black or brown limonite showed that four mass-loss steps were obtained for the black, massive limonite (Figure 5a). Approximately 0.17% and 3.08% of the mass was lost when the temperature increased to 42ºC and 155ºC, respectively. The greatest mass loss of 8.36% was observed at 291ºC, when dehydroxylation of goethite and hematite occurred. Finally, 2.81% of the mass was lost at 800ºC from residual structural water. Because goethite is not transformed to hematite directly during the 155−291ºC stage, protohematite was formed instead (Gualtieri and Venturelli, 1999). Five mass-loss steps were recorded for the loose, black, radial limonite

Table 2. LA-ICP-MS analysis results (wt.%) of residual ilvaite in the dense, black, radial limonite from the Yeshan iron deposit.

	YS-13-1 Av(4)	YS-13-2 Av(4)	YS-14-1 Av(4)	YS-14-2 Av(3)
SiO_2	29.51	29.57	29.26	30.02
Al_2O_3	0.17	0.26	0.12	0.11
FeO*	49.38	49.25	47.10	46.91
MnO	4.24	4.58	6.69	6.66
MgO	0.11	0.16	0.71	0.54
CaO	15.08	14.69	14.67	14.34
Total	98.48	98.50	98.54	98.58
Based on 6 cations and 8.5 oxygens				
Si^{4+}	1.95	1.95	1.92	1.97
Al^{3+}	0.01	0.02	0.01	0.01
Fe^{3+}	1.09	1.08	1.14	1.04
Fe^{2+}	1.63	1.64	1.45	1.54
Mn^{2+}	0.24	0.26	0.37	0.37
Mg^{2+}	0.01	0.02	0.07	0.05
Ca^{2+}	1.07	1.04	1.03	1.01
Sum	6.00	6.00	6.00	6.00

Note: FeO* was the total amount of Fe, partitioned between Fe^{2+} and Fe^{3+}, was calculated in order to ensure charge neutrality. H_2O was not determined.

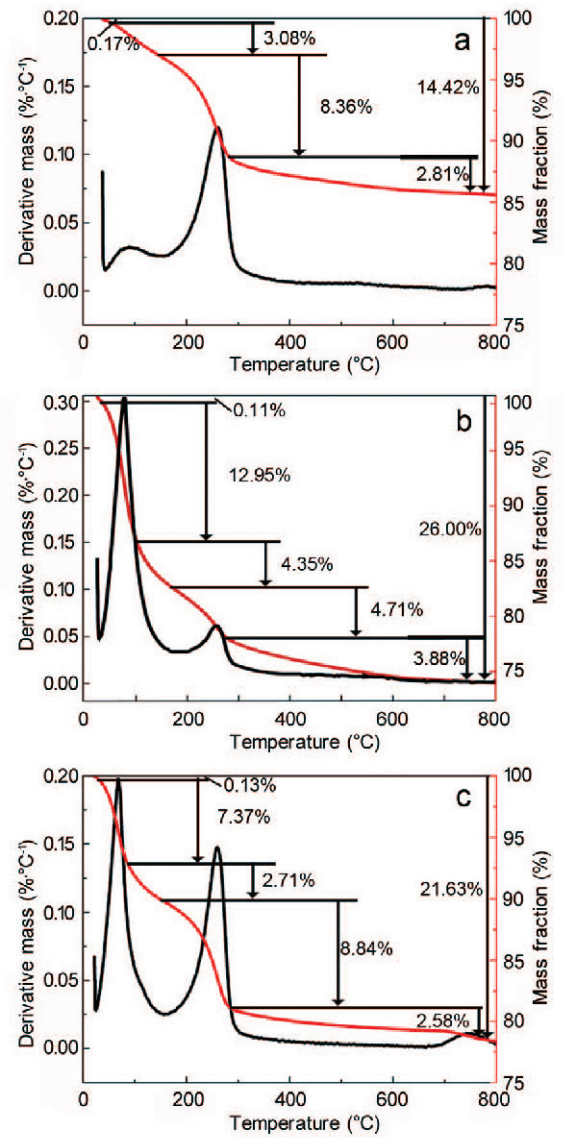

Figure 5. TG analysis results of limonite: (a) dense, black, massive limonite; (b) loose, black, radial limonite; (c) loose, brown limonite.

https://doi.org/10.1346/CCMN.2018.064102a Published online by Cambridge University Press

(Figure 5b). Three mass-loss steps (0.11%, 12.95%, and 4.39%) were found when the temperature increased to 161ºC, but only 4.71% of mass was lost when the temperature reached 287ºC. This is attributed to the loss of structural water. Beyond 287ºC, 3.88% of mass was lost due to the transformation of protohematite to hematite. Similar results were found for the brown limonite (Figure 5c) as for natural goethite (Liu *et al*., 2013), except for more adsorbed water in the brown limonite.

FE-SEM. The FE-SEM images show that goethite in the black, massive limonite (Figures 6a,b, 7a) is present as nanoparticles with no distinct crystal morphology, with moderate Mn content, and with low Si and Al contents. In the loose, black, radial limonite (Figures 6c,d, 7b), submicron-scale acicular goethite was arranged in fasciculate aggregates, with open spaces generated, making the limonite softer. The acicular goethite had a large Mn content and small Al content. In the brown limonite (Figure 6e,f, 7c), goethite also had an acicular morphology, but the crystals were longer, while aggregates were either fasciculate or honeycomb, this goethite's chemical composition was purer. Based on EDS, the Mn content was greater than that of Fe, indicating that Mn-oxide minerals may exist in the black limonite (Figures 6c,g, 7d). Some Fe-Mn oxides/hydroxides existed on the ilvaite surface (Figures 6g,i, 7e,f), making the flat surface rougher.

TEM

The TEM images show that nanoparticles (<15 nm) of goethite were present in the black, massive limonite (Figure 8a), but well developed acicular crystals had not formed. In the loose, black, radial limonite, single goethite crystals were 50–100 nm long and ~10 nm wide on average (Chen *et al*., 2017), showing a maximum ratio of length/width. In the brown limonite (Figure 8b), complete acicular goethite crystals were 100–400 nm long, and 30–60 nm wide.

The HRTEM indicated that goethite in the black limonite, with faces at (130), (221), and (140), had distinct lattice defects (Figure 8c), and some (such as the (111) face) were surrounded by amorphous material (Figure 8d). A previous study indicated that Mn oxide minerals in the loose, black radial limonite were intergrown with goethite at the nano-scale by the elemental mapping of TEM (Chen *et al*., 2017). Nevertheless, in the black limonite, groutite was confirmed by fast-Fourier Transform (FFT) analysis of HRTEM lattice fringes (Figure 8e), a pyrolusite particle was identified by means of its two crystal faces (210) and ($1\bar{2}0$) with an angle of 90º (Figure 8f), and a ramsdellite particle was confirmed by means of its two crystal faces (210) and (400) with an angle of 121º (Figure 8g).

Furthermore, the acid-insoluble components of the black limonite were interpreted as amorphous silica with no lattice fringes (Figure 8h,i), while d = 0.18 nm, the (024) lattice fringe of hematite, meant that minor hematite existed in the black limonite, due to the very limited solubility of hematite in the solution.

DISCUSSION

Mineral compositions of limonite

Following mineralogical and petrographic analysis by XRD, FE-SEM, and TEM, limonite in the Yeshan iron deposit has been found to consist mainly of goethite (or Mn-goethite), Mn-oxide minerals, amorphous phases, with minor coexisting quartz, hematite, ilvaite, and pyrite.

The XRF and EDS indicated large Mn contents in the black limonite while no Mn was found in the brown limonite. Previous studies have reported that replacement of Fe by Mn in goethite changes its color from yellow to darker colors (Alvarez *et al*., 2015) suggesting that the Mn content can affect the color of limonite. Goethite occurs commonly in supergene weathering deposits (Li, J.W. *et al*., 2007; Essalhi *et al*., 2011; Liu *et al*., 2014; Andreu *et al*., 2015), and is distributed widely in soil sediments, rivers, and lakes (Cornell and Schwertmann, 2003). The morphologies (acicular, nodular, globular, platey, and flaky) are probably controlled by the growing space, the supply of materials, and the growth rate (Mohapatra *et al*., 2008). Goethite in the present study was found to be either granular or acicular, and these forms might relate to its spatial occurrence. On the one hand, when ilvaite weathers in the inner ore body, nanoparticles of goethite form within the crystal of the parent mineral (pseudo-goethite). On the other hand, adequate space and water (supplied by rain) for the growth of goethite result in acicular crystal forms of goethite on the exterior of the ore body. When sulfides weather, Si and Mn do not affect the lattice dimensions of goethite, nor does the crystallization. The brown limonite is, therefore, characterized by well developed, larger acicular goethite.

Secondary Mn oxides are abundant in the shallow surface, *e.g.* pyrolusite, ramsdellite, cryptomelane, todorokite, and chalcophanite (Ostwald, 1988; Post, 1999; Baioumy *et al*., 2013). Pyrolusite, ramsdellite, and groutite in the black limonite were identified by HRTEM, and the total amounts of Mn oxides present were found to be 23.98% and 28.31% in the black, massive, or radial limonite, respectively (Table 3). Ramsdellite can be formed by low-temperature hydrothermal activity (Post, 1999), but the majority of it is found in superficial deposits, and is interpreted as having formed by the transformation of groutite, nsutite, or cryptomelane *via* solid-phase alteration (Nahon *et al*., 1984; Miura *et al*., 1990). Groutite is reported as being isostructural with goethite, as is ramsdellite (Post, 1999; Scheinost *et al*., 2001). The greater the degree of Mn replacement, the closer the unit-cell parameters of

https://doi.org/10.1346/CCMN.2018.064102a Published online by Cambridge University Press

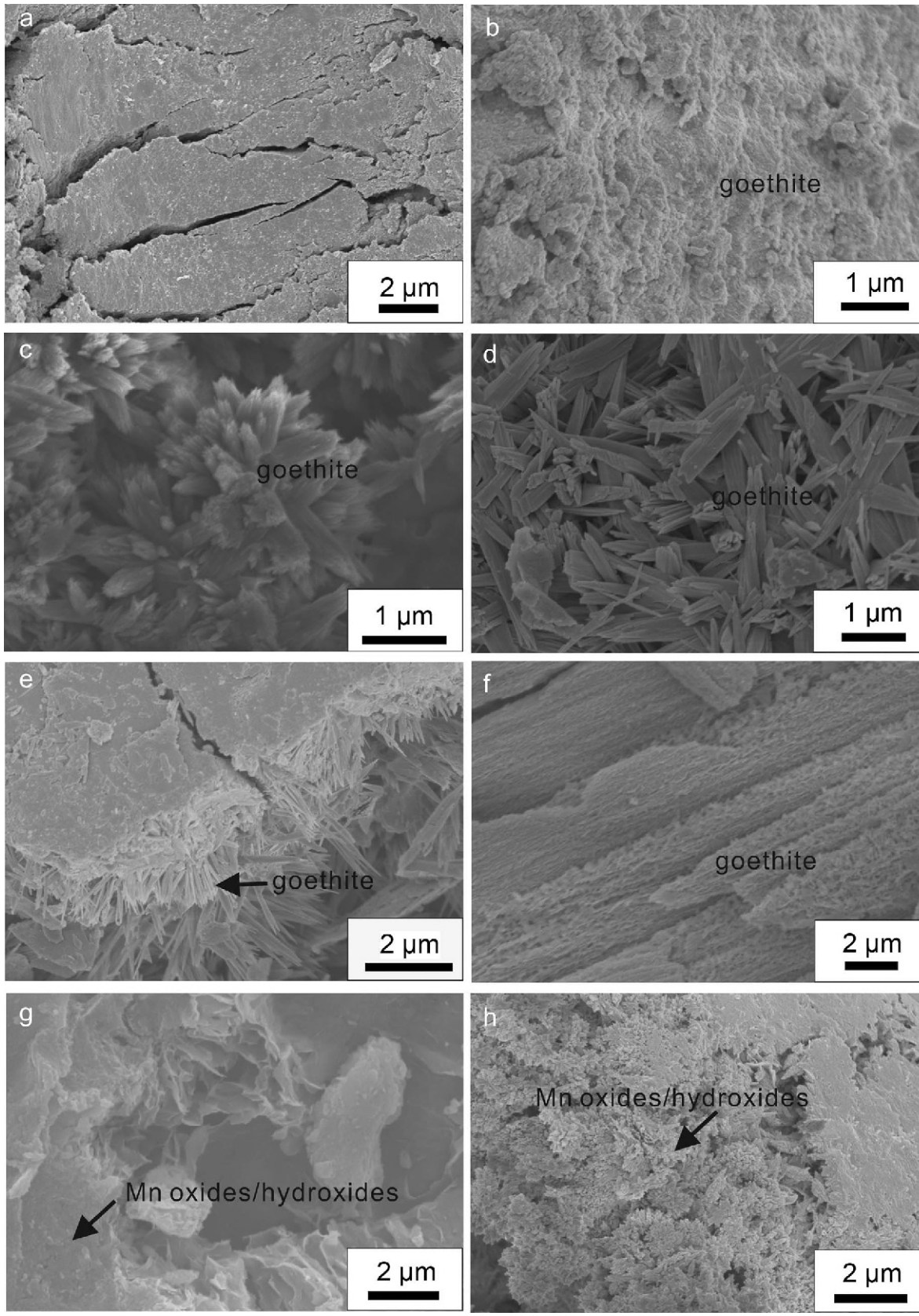

https://doi.org/10.1346/CCMN.2018.064102a Published online by Cambridge University Press

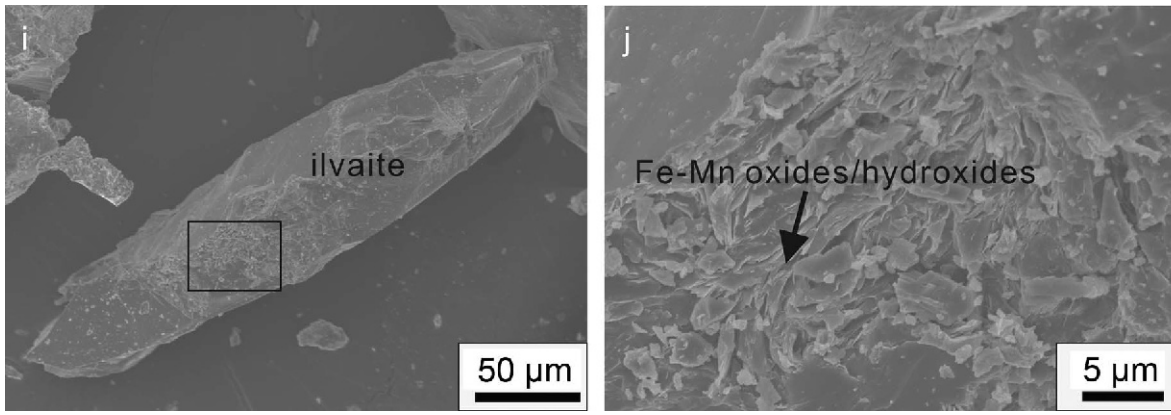

Figure 6 (*above and facing page*). FE-SEM images showing: (a, b) nano-granular goethite in the dense, black, massive limonite; (c, d) goethite in the loose, black, radial limonite is acicular and radial in aggregates; (e, f) goethite in the loose, brown limonite is acicular and is associated with granular goethite and has a honeycomb texture in aggregates; (g, h) Mn oxides/hydroxides associated with goethite; (i, j) ilvaite and some foliated Fe-Mn oxides/(oxy)hydroxides adhered to its surface.

goethite will be to that of groutite, until a goethite–groutite solid solution forms. At higher pH, groutite transforms to ramsdellite, which eventually forms the more stable pyrolusite. The fact that Mn oxides are only present as nanoparticles may be related to this growth mechanism, rather than the direct precipitation of the manganese ion, and the mineral assemblages also suggest that the pH value of the environment is from acidic to alkaline.

The amount of acid-insoluble phases decreased from black, radial limonite to black, massive limonite to brown limonite: 12.64 wt.%, 8.65 wt.%, and 3.66 wt.%, respectively (Table 3). Small amounts of quartz or hematite were inferred from the XRD patterns, meaning that nearly all the silica was amorphous. But XRF measurements detected a smaller amount of SiO_2, probably due to the fact that amorphous silica had a lot of adsorbed water. The acid-insoluble phase is formed from silicon-oxygen tetrahedra in the ilvaite, which leach little during weathering, while few or no clay minerals are formed during weathering due to a lack of Al anions and of Mg, Na, and K cations. Al-poor and Fe-enriched clay minerals, such as nontronite, have been found extensively in weathered basalt and ultrabasic rocks (Koch *et al*., 1995), and in hydrothermal sediments with Mn oxides and limonite (Dymond *et al*., 1980; Barrett and Friedrichsen, 1982; Singer *et al*., 1984); furthermore, studies of synthetic nontronite have indicated that the experimental conditions were low temperature (15−96ºC), low oxidation-reduction potential, and moderate pH (Harder, 1976, 1977, 1978; Carlo *et al*., 1983); but the mine water is usually more acidic and oxygen-rich which means that it is probably not suitable for the growth of nontronite. Opal cannot form either because the existence of large Fe and Mn contents might prevent the agglomeration of Si (Conrad *et al*., 2007). Instead, mass amorphous silica observed in the limonite, is apparently different from the observations in siderite or sulfides-weathered limonite (Liu *et al*., 2016). Hence, the presence of amorphous silica in limonite is evidence of its origin from weathering of skarn minerals (a series of silicate minerals originating from contact-metamorphism minerals such as epidote, garnet, and ilvaite).

Ilvaite weathering and limonite formation

Ilvaite is unstable in acidic conditions (Pellant, 1992) which means that it weathers readily in a supergene environment. When sulfides, such as pyrite, dissolve first, the resulting Fe^{2+}, SO_4^{2-}, and H^+ ions reduce the pH of the aqueous solution. This leads to the formation of fractures in ilvaite and eventually dissolution of the crystal. At this stage, Ca is released first, then SiO_2, while Fe and Mn remain with the residual SiO_2. Fe^{2+} and Fe^{3+} finally form goethite through a series of reactions (Dubiková *et al*., 2002; España *et al*., 2005; Burgos *et al*., 2012). Previous studies have shown that the optimal pH for the formation of Mn-goethite or Fe-groutite is 4 to 6 (Ebinger, 1989). Because the radius of Mn^{3+} is similar to that of Fe^{3+} (Güner, 2015), Mn^{3+} can easily replace Fe^{3+} to form Mn-goethite in an acidic environment. Fe-groutite is formed in the presence of excess Mn and eventually transforms to ramsdellite and pyrolusite. SiO_2 and pH are the two key factors which lead to the unique structure in the skarn minerals weathered to limonite: the former can prevent the transformation of ferrihydrite to goethite, or the growth of crystals, and decrease their crystallinity (Cornell, 1987; Wang *et al*., 2015) so that poorly crystallized or amorphous iron phases were well developed according to Table 3. This is probably due to an ambient aqueous solution rich in silicate after an ilvaite crystal dissolved, and the precursor of some silicic acid generates amorphous silicon by dehydration during evolution; besides, a suitable environment for the evolution of Fe-Mn-Si from low pH to high pH can be envisaged. Limonite

https://doi.org/10.1346/CCMN.2018.064102a Published online by Cambridge University Press

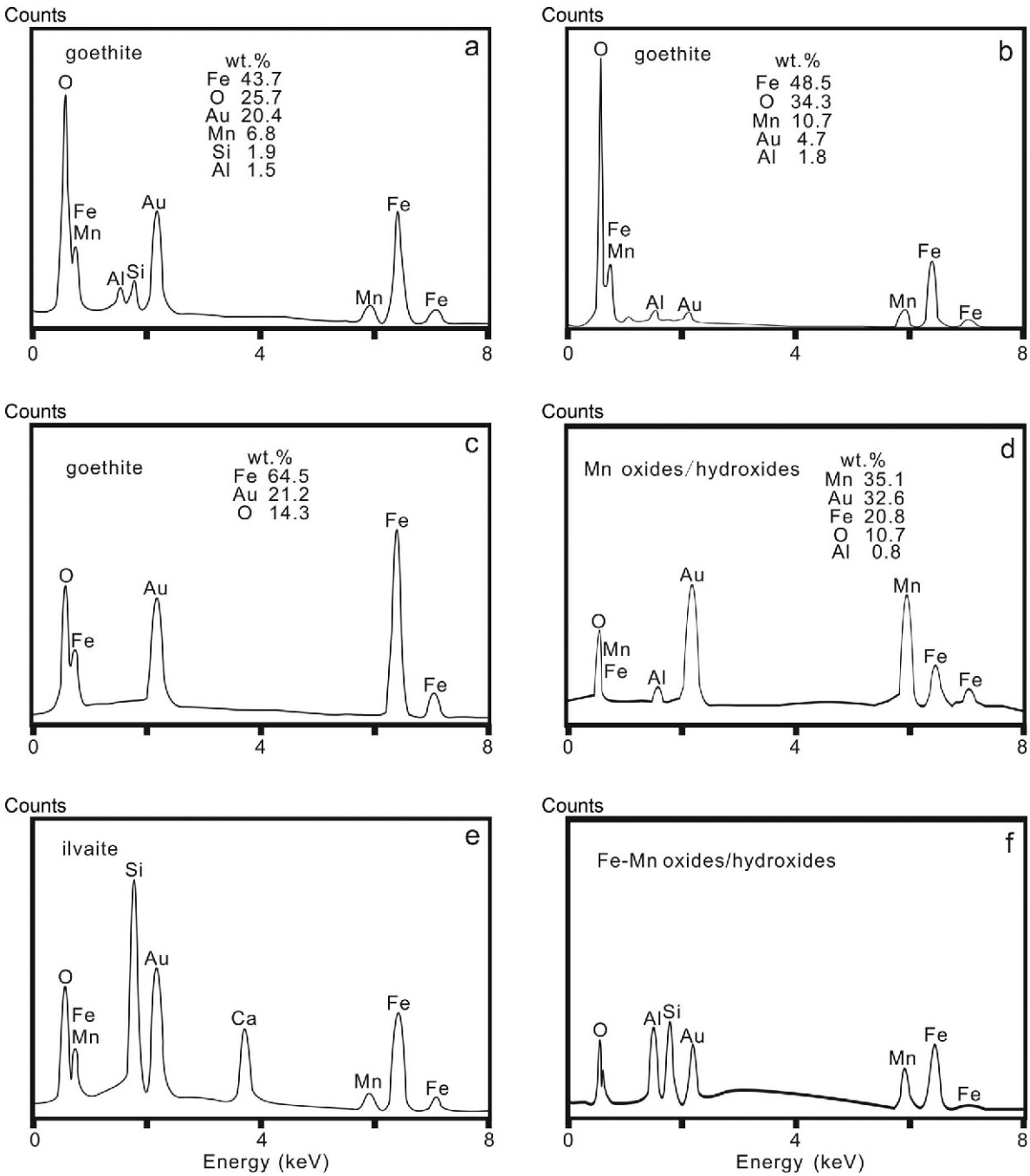

Figure 7. EDS analyses of material shown in the FE-SEM images in Figure 6: (a–c) goethite; (d) Mn oxides/hydroxides; (e) ilvaite; (f) Fe-Mn oxides/(oxy)hydroxides.

formed under these conditions, therefore, has a unique microstructure compared to the coprecipitated Fe-Mn-Si oxide (Maeng *et al*., 2013), or the Fe-Mn-Si oxides of hydrothermal origin (Taitel-Goldman *et al*., 2009; Sun *et al*., 2012). The Fe and Mn contents of skarn minerals are the primary factors that control whether goethite can form limonite or not. Si and Al contents are important factors in determining whether limonite is pure. Hence, for silicates that are rich in Si and Al, but poor in Fe and Mn, *e.g.* diopside, their weathering products are usually clays or opal with minor goethite (Colin *et al*., 1990; Tripathi and Rajamani, 2007; Michael *et al*., 2010); for Al-poor silicate minerals, as long as Al can be supported by the environment, this cannot be called 'limonite.' For Mn-bearing ilvaite, Ca and Mg are lost during the weathering process, increasing the relative average

https://doi.org/10.1346/CCMN.2018.064102a Published online by Cambridge University Press

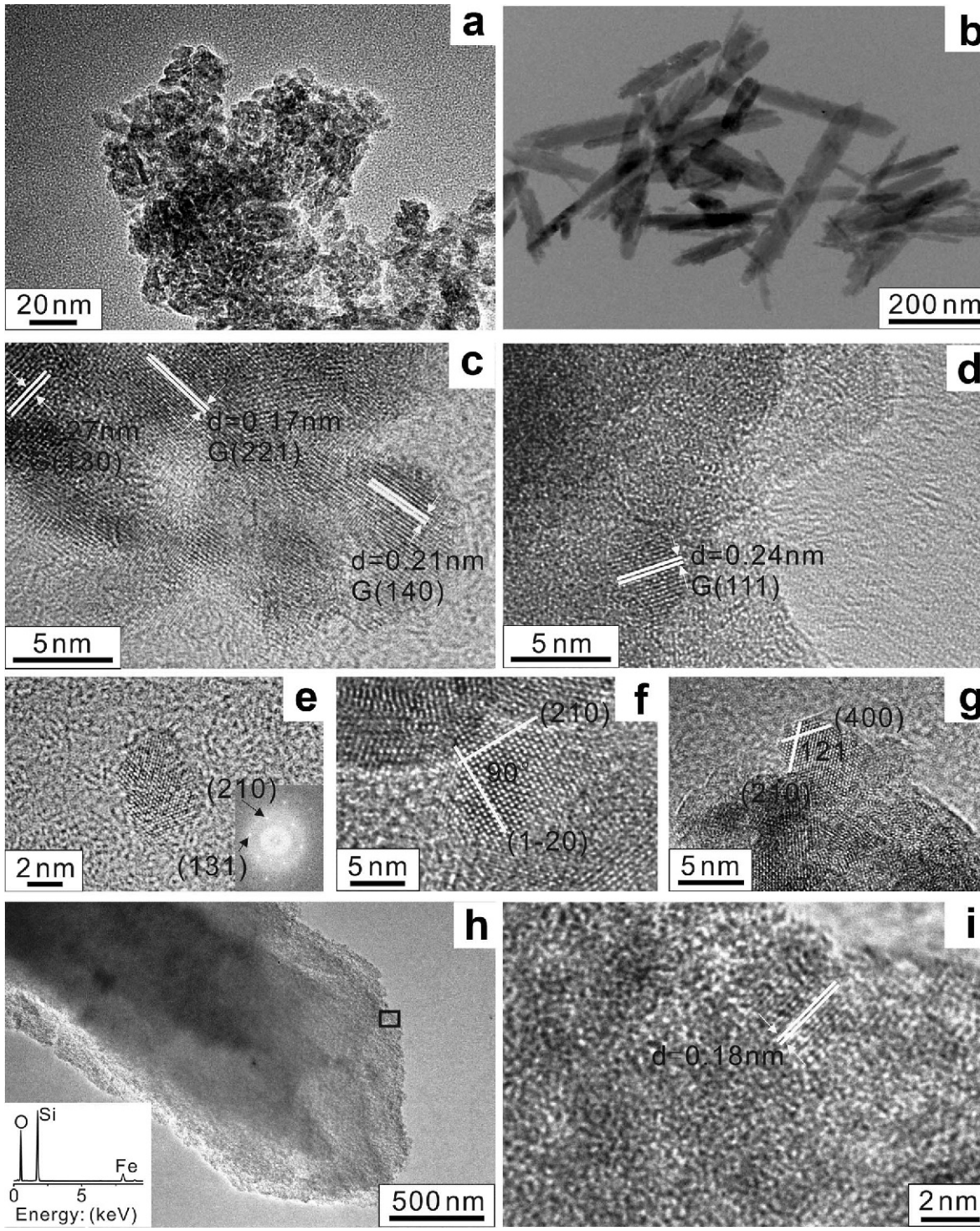

Figure 8. (a) TEM image of nano-granular goethite in the dense, black, massive limonite; (b) TEM image of acicular goethite in the loose, brown limonite; (c) HRTEM image of various faces of goethite with lattice defects; (d) HRTEM image of goethite surrounded by amorphous Fe-Mn phases; (e) HRTEM image of groutite with inset FFT of the HRTEM image in the lower right corner; (f) HRTEM image of a single pyrolusite crystal shows 0.19 nm (210) and 0.19 nm ($1\bar{2}0$) lattice fringes; (g) HRTEM image of a single ramsdellite crystal shows 0.24 nm (400) and 0.25 nm (210) lattice fringes; (h) TEM image of materials insoluble in acid with EDS results of the selected area inserted in the lower left; (i) HRTEM image of the selected area in the left image.

https://doi.org/10.1346/CCMN.2018.064102a Published online by Cambridge University Press

Table 3. Quantitative analysis (%) of mineral constituents in limonite from the Yeshan iron deposit.

	Mn oxides[1]	Poorly crystallized or amorphous Fe phases[2]	Amorphous silica and quartz, hematite[3]
Dense, black, massive limonite	23.98	17.71	8.65
Loose, black, radial limonite	28.31	30.86	12.64
Loose, brown limonite	0.08	13.75	3.66

Notes: every experiment was repeated three times and the results averaged.
[1] Mn oxide contents extracted using 0.1 M hydroxylamine hydrochloride solution.
[2] Surplus dissolved quantity extracted by 0.2 M oxalic acid/0.2 M ammonium oxalate solution minus the Mn oxides content.
[3] Amount of insolubles in acid extracted by 0.1 M hydroxylamine hydrochloride solution, of which solvent was 20% hydrochloric acid.

values of Fe and Mn contents to 64.37 wt.% from 53.71 wt.% (not considering the loss of Si). The lack of a distinct correlation between SiO_2 and Al_2O_3 (Figure 9a) may indicate a lack of clay minerals; this limonite has the advantage of very few clay-mineral impurities and a pure chemical composition. The chemical compositions of Yeshan limonite, which show a relative lack of Mg, Na, or Al, may also imply a semi-enclosed environment for the growth of secondary minerals.

Slight differences in chemical composition between the two kinds of black limonite can be found. First, the loose, black, radial limonite had greater Si, Al, Ca, Cu, Zn, and Ba contents than the black, massive limonite. No Cu, Zn, or Ba was detected in the ilvaite, however, though these elements may be derived from some sulfide minerals. Because (1) pyrite is intergrown with ilvaite as shown by in Figure 3d) and (2) the amount of amorphous silica (~3.66%, see Table 3) is very small in the brown limonite, limonite, with two different colors and a strange distribution results from the inheritance of the relationship between sulfides and ilvaite. Given the combination of Mn-bearing ilvaite identified by previous studies, and the microscopic images of ilvaite, or the chemical composition of black limonite from the present study, mineral assemblages of ilvaite, pyrite ± sphalerite, gelenite, manganhedenbergite, and bustamite may be presumed (Zhao *et al.*, 1990). If this is the case, the weathering products of ilvaite, manganhedenbergite, and bustamite will be indistinguishable, as their chemical compositions are similar (Zhao *et al.*, 1983).

Second, black limonite had different water contents, which can reflect differences in mineral composition, structure, and spatial distribution. The black, massive limonite had less adsorbed water, but more structural water than the loose, black, radial limonite. Moderate amounts of structural water and adsorbed water were detected in the brown limonite. The black, massive limonite might have less adsorbed water because goethite grown at greater depths did not have enough space to develop an acicular structure, these nano particles lead to the formation of a dense, low-permeability structure, further hindering the water support from outside for crystal growth. At the surface, with enough space for goethite to grow, acicular goethite crystals increased the porosity in the limonite, increasing the contact between minerals and water, thus facilitating adsorption. Furthermore, a large amount of amorphous Fe-Mn phases may reduce the structural water content, but amorphous phases are more effective at the adsorption of adsorbed water. Besides, the negative correlations between (Fe_2O_3+MnO) and (CuO+ZnO+BaO) or between (Fe_2O_3+MnO) and Al_2O_3 (Figure 9b,c) may also support the above conclusions.

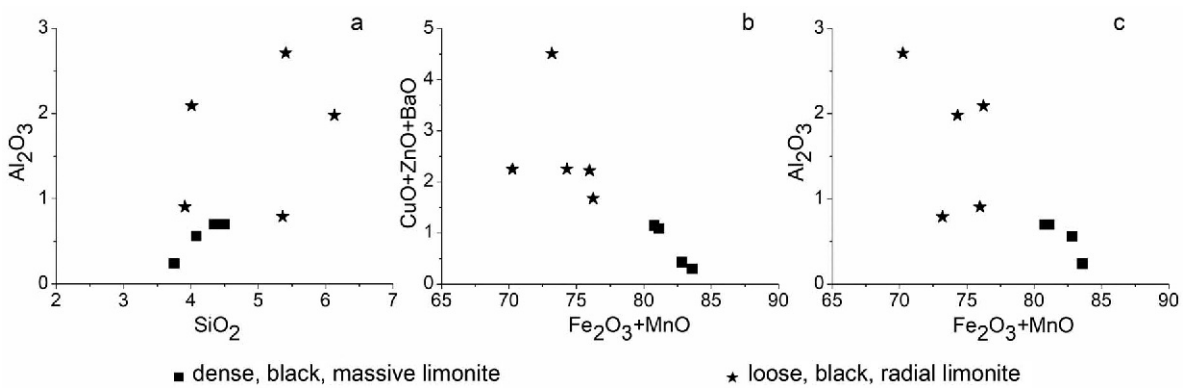

Figure 9. Elemental variation diagrams for major oxides (wt.%) of the dense, black, massive limonite and loose, black, radial limonite. (a) SiO_2 *vs.* Al_2O_3; (b) Fe_2O_3 + MnO *vs.* CuO + ZnO + BaO; (c) Fe_2O_3 + MnO *vs.* Al_2O_3.

https://doi.org/10.1346/CCMN.2018.064102a Published online by Cambridge University Press

Significance of studies on the characteristics and genesis of limonite

According to Li *et al.* (1992), Liu (2016), and further observation of different genetic types of limonite, parent rocks can be distinguished in several ways. Generally speaking, in sulfides weathered to limonite, sulfate minerals, such as jarosite and beudantite (Figures 10a, 11a), and baryte (Figures 10b, 11b) are accompanied by goethite; smithsonite (Figures 10c, 11c) or hetaerolite (Figures 10d, 11d) may also develop in both sulfides and siderite weathered to limonite; clay minerals (such as illite) (Figures 10e, 11e) and Mn oxide (Figures 10f, 11f) appear in the siderite weathered to limonite. Sometimes, Mn oxides and clay minerals may also appear in the skarn mineral weathered to limonite; but, in the siderite weathered to limonite, Mn oxides tend to be larger, and no special microstructure can be found between the Fe/Mn minerals as the pH is greater in the presence of CO_3^{2-}, so Mn oxides form directly from the system; and clay minerals are found as a residue, these making apparent differences in the micromorphology.

Limonite is not only widely distributed in the Tongling ore concentration area, but also in the middle–lower Yangtze Valley metallogenic belt (Li *et*

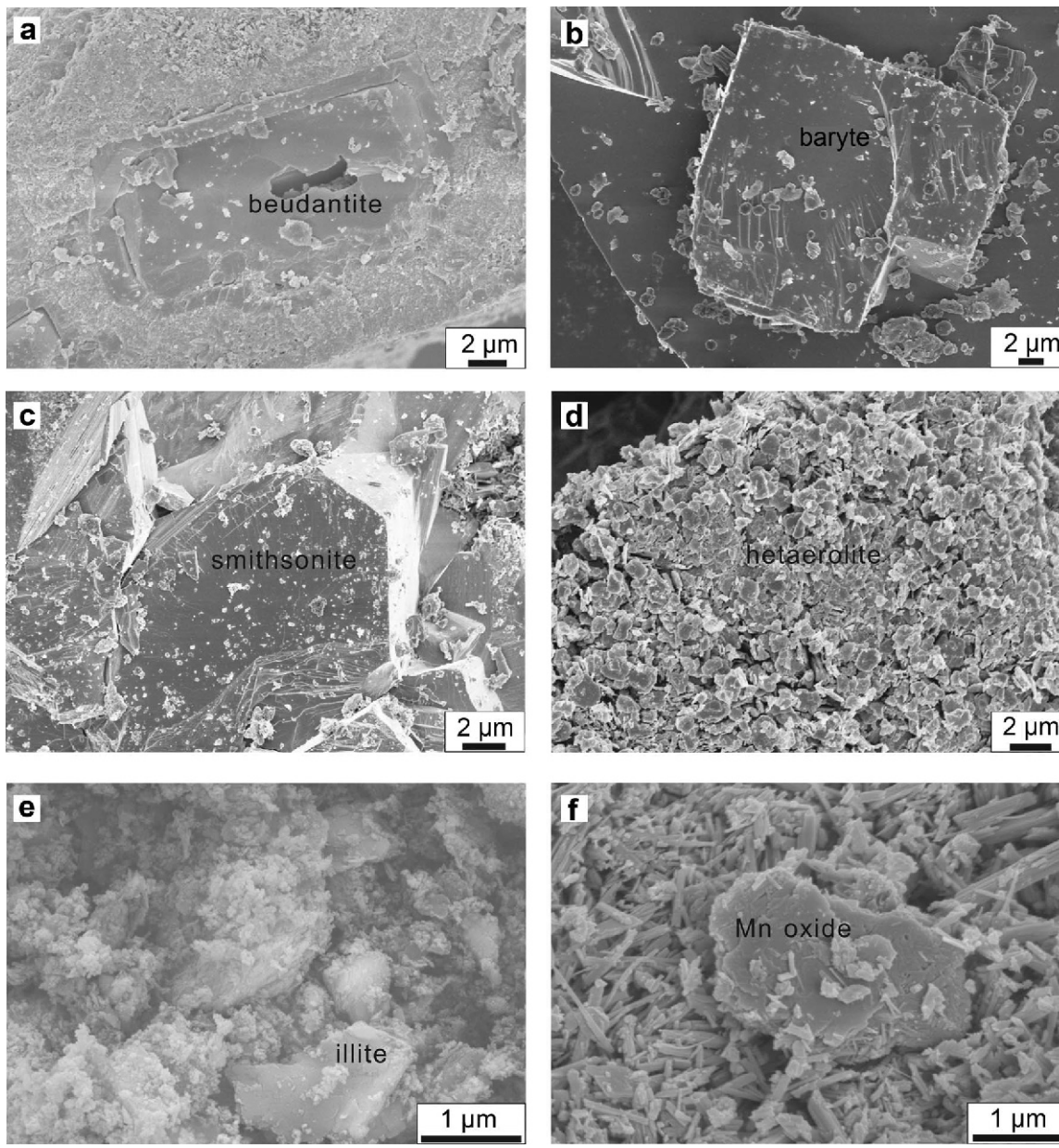

Figure 10. FE-SEM images of different minerals in the sulfides weathered to limonite or the siderite weathered to limonite: (a) beudantite; (b) baryte; (c) smithsonite; (d) hetaerolite; (e) illite; (f) Mn oxide.

https://doi.org/10.1346/CCMN.2018.064102a Published online by Cambridge University Press

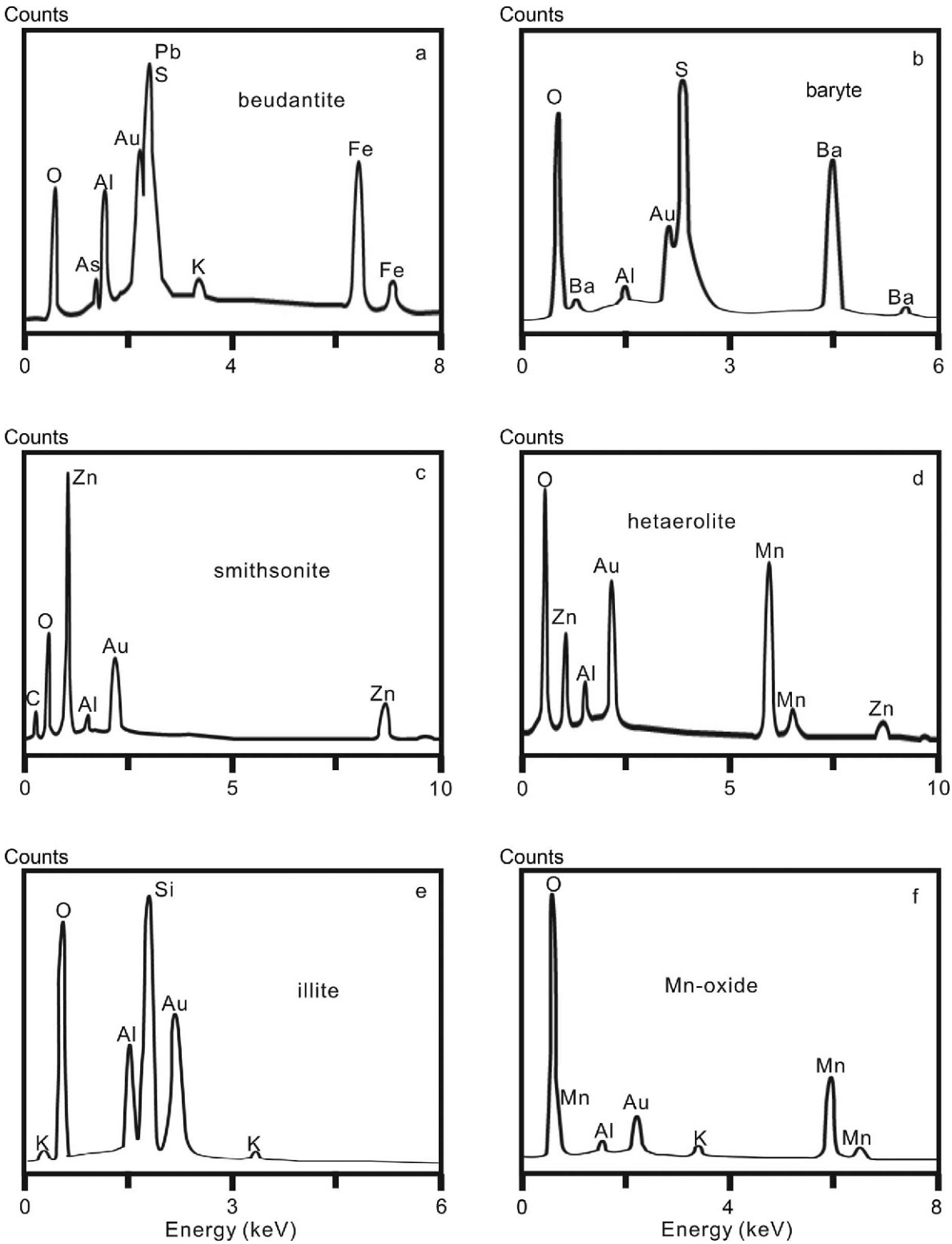

Figure 11. EDS analyses of FE-SEM (Figure 10): (a) beudantite; (b) baryte; (c) smithsonite; (d) hetaerolite; (e) illite; (f) Mn oxide.

al., 1992). In the past, limonite was regarded as an indicator when prospecting for Pb-Zn sulfide deposits or for gold ore. Because of its considerable reserves but inconsistent with the resource value, recent attempts

https://doi.org/10.1346/CCMN.2018.064102a Published online by Cambridge University Press

have also been made to use it in the environmental engineering field. Uses of limonite are very restricted, however, due to the lack of related studies on its mineral properties, its various geneses, and its different characteristics in terms of mineralogy, chemical composition, and microstructure. Studies have shown, nevertheless, a high efficiency of black limonite in the removal of nitrogen due to the catalytic oxidation properties of the Mn oxides. Systematic mineralogical studies of limonite will not only enable a better understanding of its environmental properties and discern its genesis, but also extend its value as a nano-mineral resource (Chen *et al*., 2017).

CONCLUSIONS

In the present study, an integrated analysis of geological, XRD, XRF, LA-ICP-MS, TG, FE-SEM, and TEM data have enabled the following conclusions to be made:

(1) The black limonite had the following main mineral assemblage: Mn-goethite, groutite, ramsdellite, and pyrolusite. Mn-goethite had low crystallinity and showed nano-granular (<15 nm) or acicular (50−100 nm long, ~10 nm wide) form. Groutite, ramsdellite, and pyrolusite were present as ~5 nm particles adhering to the surfaces of larger particles. Much of the amorphous silica and amorphous Fe-Mn phases were highly developed. Ilvaite, quartz, and hematite were also found in some samples; Fe/Mn oxides and (oxy)hydroxides were found on the edges of ilvaite, indicating a replacement relationship between them. The average ilvaite structural formula was $Ca_{1.04}(Fe_{1.57}Mn_{0.31}Mg_{0.04})(Fe_{1.09}Al_{0.01})$ $[Si_{1.95}O]O(OH)$.

(2) The black limonite had variable adsorbed water or structural water content, relatively large CuO, ZnO values, small Al_2O_3 contents, and very small amounts of CaO. The analyses cited above, combined with the negative correlations between (Fe_2O_3+MnO) and (CuO+ZnO+BaO), (Fe_2O_3+MnO) and Al_2O_3, and the large Mn, Si contents, between the black limonite and ilvaite suggest that black limonite was formed from ilvaite weathering in a semi-enclosed environment, and was greatly affected by the spatial distribution; acidic to weakly alkaline conditions were deduced for the crystal growth.

ACKNOWLEDGMENTS

The present research was supported financially by the National Science Foundation of China (41572029, 41672038, and 41372046). The authors are grateful to Zhang Qiang, Wang Yang, and Wang Fangyue who helped with the FE-SEM, TEM, and LA-ICP-MS analyses.

REFERENCES

Abe, H. (1972) Chemical compositions of altered rocks surrounding volcanogenic limonite deposits of the Abuta mine, Hokkaido. *The Journal of the Japanese Association of Mineralogists, Petrologists and Economic Geologists*, **67**, 352−356.

Agata, T. and Adachi, M. (1995) Ilvaite from a serpentinized peridotite in the Asama igneous complex, Mikabu greenstone belt, Sambagawa metamorphic terrain, central Japan. *Mineralogical Magazine*, **59**, 489−496.

Alvarez, M., Sileo, E.E., and Rueda, E. H. (2005) Effect of Mn (II) incorporation on the transformation of ferrihydrite to goethite. *Chemical Geology*, **216**, 89−97.

Alvarez, M., Tufo, A.E., Zenobi, C., Ramos, C.P., and Sileo, E.E., (2015) Chemical, structural and hyperfine characterization of goethites with simultaneous incorporation of manganese, cobalt and aluminum ions. *Chemical Geology*, **414**, 16−27.

Andreu, E., Torró, L., Proenza, J.A., Domenech, C., García-Casco, A., Benavent, C.V.D., Chavez, C., Espaillat, J., and Lewis, J.F. (2015) Weathering profile of the Cerro de Maimón VMS deposit (Dominican Republic): textures, mineralogy, gossan evolution and mobility of gold and silver. *Ore Geology Reviews*, **65**, 165−179.

Baioumy, H.M., Khedr, M.Z., and Ahmed, A.H. (2013) Mineralogy, geochemistry and origin of Mn in the high-Mn iron ores, Bahariya Oasis, Egypt. *Ore Geology Reviews*, **53**, 63−76.

Barrett, T.J. and Friedrichsen, H. (1982) Elemental and isotopic compositions of some metalliferous and pelagic sediment from the Galapagos Mounds area, DSDP Leg 70. *Chemical Geology*, **36**, 275−298.

Blanchard, R. and Boswell, P.F. (1935) "Limonite" of molybdenite derivation. *Economic Geology*, **30**, 313−319.

Bonev, I.K., Vassileva, R.D., Zotov, N., and Kouzmanov, K. (2005) Manganilvaite, $CaFe^{2+}Fe^{3+}(Mn, Fe^{2+})(Si_2O_7)O(OH)$, a new mineral in the ilvaite group, from Pb-Zn skarn deposits in the Rhodope Mountains, Bulgaria. *The Canadian Mineralogist*, **43**, 1027−1042.

Bowell, R.J. (2010) Sulfide oxidation and production of gossans, Ashanti mine, Ghana. *International Geology Review*, **36**, 732−752.

Burgos, W.D., Borch, T., Troyer, L.D., Luan, F., Larson, L.N., Brown, J.F., Lambson, J., and Shimizu, M. (2012) Schwertmannite and Fe oxides formed by biological low-pH Fe (II) oxidation versus abiotic neutralization: impact on trace metal sequestration. *Geochimica et Cosmochimica Acta*, **76**, 29−44.

Bustamante, A., Cabrera, J., Garcia, V., Urday, E., Abdu, Y.A., and Scorzelli, R.B. (2005) Mössbauer spectroscopy description of limonite from Taraco, in the Huancane province of the Puno region, Peru. *Hyperfine Interactions*, **166**, 593−597.

Cai, J.H. (2006) Gold occurrence in a gossan type gold deposit in Tongling, Anhui. *Mineral Resources and Geology*, **20**, 283−286 (in Chinese).

Cao, X.S. and Kong, D.F. (1991) Zoning characterics and metallogeny of the gossan gold deposit at Xinqiao, Tongling, Anhui. *Contributions to Geology and Mineral Resources Research*, **6**, 71−79 (in Chinese).

Carlo, E.H.D., McMurtry, G.M., and Yeh, H.W. (1983) Geochemistry of hydrothermal deposits from Loihi submarine volcano, Hawaii. *Earth and Planetary Science Letters*, **66**, 438−449.

Chen, P., Chen, T.H., Xu, L., Liu, H.B., and Xie, Q.Q. (2017) Mn-rich limonite from the Yeshan Iron Deposit, Tongling District, China: A natural nanocomposite. *Journal of Nanoscience and Nanotechnology*, **17**, 6931−6935.

Colin, F., Nahon, D., Trescases, J.J., and Melfi, A.J. (1990) Lateritic weathering of pyroxenites at Niquelandia, Goias, Brazil: the supergene behavior of nickel. *Economic Geology*, **85**, 1010−1023.

Conrad, C.F., Icopini, G.A., Yasuhara, H., Bandstra, J.Z.,

Brantley, S.L., and Heaney, P.J. (2007) Modeling the kinetics of silica nanocolloid formation and precipitation in geologically relevant aqueous solutions. *Geochimica et Cosmochimica Acta*, **71**, 531–542.

Cornell, R.M. (1987) Effect of silicate species on the transformation of ferrihydrite into goethite and hematite in alkaline media. *Clays and Clay Minerals*, **35**, 21–28.

Cornell, R.M. and Schwertmann, U. (2003) *The Iron Oxides: Structure, Properties, Reactions, Occurrences and Uses*. Wiley-VCH, Germany, pp. 433–475.

Dubiková, M., Cambier, P., Šucha, V., and Čaplovičová, M. (2002) Experimental soil acidification. *Applied Geochemistry*, **17**, 245–257.

Dymond, J., Corliss, J.B., Cobler, R., Muratli, C.M., Chou, C., and Conard, R. (1980) Composition and origin of sediments recovered by deep drilling of sediment mounds, Galapagos Spreading Center. In *Initial Reports of Deep Sea Drilling Project,* **Vol. 54**, (B.R. Rosenthal *et al*., editors). U.S. Government Printing Office, Washington D.C., pp. 377–385.

Ebinger, M.H. (1989) Mn-substituted goethite and Fe-substituted groutite synthesized at acid pH. *Clays and Clay Minerals*, **37**, 151–156.

Embrechts, J. and Stoops, G. (1982) Microscopical aspects of garnet weathering in a humid tropical environment. *European Journal of Soil Science*, **33**, 535–545.

Endo, S. (2017) Ilvaite–manganilvaite series minerals in jasper and iron–manganese ore from the Northern Chichibu belt, central Shikoku, Japan. *Journal of Mineralogical and Petrological Sciences*, 112, 166–174.

España, J.S., Pamo, E.L., Santofimia, E., Aduvire, O., Reyes, J., and Barettino, D. (2005) Acid mine drainage in the Iberian Pyrite Belt (Odiel river watershed, Huelva, SW Spain): geochemistry, mineralogy and environmental implications. *Applied Geochemistry*, **20**, 1320–1356.

Essalhi, M., Sizaret, S., Barbanson, L., Chen, Y., Lagroix, F., Demory, F., Nieto, J.L., Saez, R., and Capitan, M.A. (2011) A case study of the internal structures of gossans and weathering processes in the Iberian Pyrite Belt using magnetic fabrics and paleomagnetic dating. *Mineralium Deposita*, **46**, 981–999.

Franchini, M.B. (2002) First occurrence of ilvaite in a gold skarn deposit. *Economic Geology and the Bulletin of the Society of Economic Geologists*, **97**, 1119–1126.

Frost, R.L., Ding, Z., and Ruan, H.D. (2003) Thermal analysis of goethite. *Journal of Thermal Analysis and Calorimetry*, **71**, 783–797.

Frisbee, N.M. and Hossner, L.R. (1995) Siderite weathering in acidic solutions under carbon dioxide, air, and oxygen. *Journal of Environmental Quality*, **24**, 856–860.

Geologic map of Tongling, Anhui Province in 1:50000 (1989) No. 321 of Bureau of Geology and Mineral Exploration of Anhui Province (in Chinese).

Gualtieri, A.F. and Venturelli, P. (1999) In situ study of the goethite-hematite phase transformation by real time synchrotron powder diffraction. *American Mineralogist*, **84**, 895–904.

Güner, S., Amir, M., Geleri, M., Sertkol, M., and Baykal, A. (2015) Magneto-optical properties of Mn^{3+} substituted Fe_3O_4 nanoparticles. *Ceramics International*, **41**, 10915–10922.

Harder, H. (1976) Nontronite synthesis at low temperatures. *Chemical Geology*, **18**, 169–180.

Harder, H. (1977) Clay mineral formation under lateritic conditions. *Clay Minerals*, **12**, 281–299.

Harder, H. (1978) Synthesis of iron layer silicate minerals under natural conditions. *Clays and Clay Minerals*, **26**, 65–72.

He, J.R., Yao, Z.Y., Li, Y., Sun, N.G., and Dai, A.H. (1992) A comprehensive exploration of gossan type gold deposit in the Middle-Lower Yangtze area. *Geology and Prospecting*, **28**, 27–33 (in Chinese).

Kaneko, T., Sugita, S., Tamura, M., Shimasaki, K., Makino, E., and Silalahi, L.H. (2002) Highly active limonite catalysts for direct coal liquefaction. *Fuel*, **81**, 1541–1549.

Kelly, W.C. (1957) Mineralogy of limonite in lead-zinc gossans. *Economic Geology*, **52**, 536–545.

Kiczka, M., Wiederhold, J.G., Frommer, J., Voegelin, A., Kraemer, S.M., Bourdon, B., and Kretzschmar, R. (2011) Iron speciation and isotope fractionation during silicate weathering and soil formation in an Alpine glacier forefield chronosequence. *Geochimica et Cosmochimica Acta*, **75**, 5559–5573.

Koch, C.B., Morup, S., Madsen, M.B., and Vistisen, L. (1995) Iron-containing weathering products of basalt in a cold, dry climate. *Chemical Geology*, **122**, 109–119.

Li, J.W., Vasconcelos, P., Duzgoren-Aydin, N., Yan, D.R., Zhang, W., Deng, X.D., Zhao, X.F., Zeng, Z.P., and Hu, M.A. (2007) Neogene weathering and supergene manganese enrichment in subtropical South China: an $^{40}Ar/^{39}Ar$ approach and paleoclimatic significance. *Earth and Planetary Science Letters*, **256**, 389–402.

Li, L., Morishita, K., and Takarada, T. (2007) Light fuel gas production from nascent coal volatiles using a natural limonite ore. *Fuel*, **86**, 1570–1576.

Li, W.D. (1980) *Studies on the Development of Oxidation of the Sulfide Ore Deposits in the Middle Lower Yangze Area.* Geological Publishing House, Beijing, China, pp. 36–117 (in Chinese)

Li, Y., He, J.R., Sun, N.G., and Yao, Z.Y. (1992) *Gossan-Type Gold Deposit of Middle-Lower Yangtze Area*. Geological Publishing House, Beijing, China, pp. 6–42 pp. (in Chinese).

Liu, H.B., Chen, T.H., Zou, X.H., Qing, C.S., and Frost, R.L. (2013) Thermal treatment of natural goethite: thermal transformation and physical properties. *Thermochimica Acta*, **568**, 115–121.

Liu, H.B., Chen, T.H., and Frost, R.L. (2014) An overview of the role of goethite surfaces in the environment. *Chemosphere*, **103**, 1–11.

Liu, S.B. (2016) *Nanomineralogy and Geochemistry of Limonite of Xinqiao Ore-field in Tongling, Anhui Province*. Masters dissertation, Hefei University of Technology, China, pp. 21–54.

Liu, T.M. (1989) Study on the properties and occurrence state of Au in the gossan gold ore from mountain Huang Shialao, Tongling City, Anhui Province. *Metallurgical Geology of Central South*, **2**, 28–33 (in Chinese).

Liu, Y.S. (2010) Continental and oceanic crust recycling-induced melt–peridotite interactions in the trans-north China orogen: U–Pb dating, Hf isotopes and trace elements in zircons from mantle xenoliths. *Journal of Petrology*, **51**, 392–399.

Liu, Y.S., Hu, Z.C., Gao, S., Günther, D., Xu, J., Gao, C.G., and Chen, H.H. (2008) In situ, analysis of major and trace elements of anhydrous minerals by LA-ICP-MS without applying an internal standard. *Chemical Geology*, **257**, 34–43.

Liu, Y.S., Hu, Z.C., Zong, K.Q., Gao, C.G., Gao, S., Xu, J., and Chen, H.H. (2010) Reappraisement and refinement of zircon U-Pb isotope and trace element analyses by LA-ICP-MS. *Science Bulletin*, **55**, 1535–1546.

Maeng, M., Lee, H., and Dockko, S. (2013) Phosphate removal using novel combined Fe-Mn-Si oxide adsorbent. *Journal of Korean Society of Water and Wastewater*, **27**, 631–639.

Michael, S., Danuta, K., Yakov, K., and Jörn, B. (2010) Silicon pools and fluxes in soils and landscapes – a review. *Journal*

of Plant Nutrition and Soil Science, **169**, 582–582.
Miura, H., Kudou, H., Choi, J.H., and Hariya, Y. (1990) The crystal structure of ramsdellite from Pirika mine. *Journal of the Faculty of Science, Hokkaido University*, **22**, 611–617.
Mohapatra, B.K., Jena, S., Mahanta, K., and Mishra, P. (2008) Goethite morphology and composition in banded iron formation, Orissa, India. *Resource Geology*, **58**, 325–332.
Nahon, D., Beauvais, A., Nziengui-Mapangou, P., and Ducloux, J. (1984) Chemical weathering of Mn-garnets under lateritic conditions in northwest Ivory Coast (West Africa). *Chemical Geology*, **45**, 53–71.
Nambu, M. (1955) Mineralogical study of limonite in Japan. *Bulletin of the Research Institute of Mineral Dressing & Metallurgy, Tohoku University*, **11**, 35–66.
Naslund, H.R., Hughes, J.M., and Birnie, R.W. (1983) Ilvaite, an alteration product replacing olivine in the Skaergaard intrusion. *American Mineralogist*, **68**, 1004–1008.
Neaman, A., Mouélé, F., Trolard, F., and Bourrié, G. (2004) Improved methods for selective dissolution of Mn oxides: applications for studying trace element associations. *Applied Geochemistry*, **19**, 973–979.
O'Connor, F., Cheung, W.H., and Valix, M. (2006) Reduction roasting of limonite ores: effect of dehydroxylation. *International Journal of Mineral Processing*, **80**, 88–99.
Okada, K., Hachiya, Y., and Kato, S. (1966) Mineralogical composition of manganiferous limonite from Kuroishi city, Aomori Prefecture. *Bulletin of the Research Institute of Mineral Dressing & Metallurgy, Tohoku University*, **21**, 135–143.
Ostwald, J. (1988) Mineralogy of the Groote Eylandt manganese oxides: a review. *Ore Geology Reviews*, **4**, 3–45.
Pellant, C. (1992) *Eyewitness Handbooks: Rocks and Minerals*. Dorling Kindersley, UK, 148 pp.
Post, J.E. (1999) Manganese oxide minerals: crystal structures and economic and environmental significance. *Proceedings of the National Academy of Sciences*, **96**, 3447–3454.
Scheinost, A.C., Stanjek, H., Schulze, D.G., Gasser, U., and Sparks, D.L. (2001) Structural environment and oxidation state of Mn in goethite-groutite solid-solutions. *American Mineralogist*, **86**, 139–146.
Sheng, G.Q. and Wang, C.Y. (1989) On the formation condition of the gold in gossans, and prospecting significance in the Tongling mining district, Anhui province. *Mineral and Exploration*, **6**, 22–26 (in Chinese).
Singer, A., Stoffers, P., Heller-Kallai, L., and Szafranek, D. (1984) Nontronite in a deep-sea core from the south pacific. *Clays and Clay Minerals*, **32**, 375–383.
Song, S., Lu, S., and Lopez-Valdivieso, A. (2002) Magnetic separation of hematite and limonite fines as hydrophobic flocs from iron ores. *Minerals Engineering*, **15**, 415–422.
Stone, J.B. (1934) Limonite deposits at the Orient mine, Colorado. *Economic Geology*, **29**, 317–329.
Sun, L. and Chu, Z.C. (2006) Study on geological characteristics, mineralization conditions and assessment criteria of gossan type gold-silver deposits in Anhui province. *Geology of Anhui*, **16**, 94–100 (in Chinese).
Sun, Z., Zhou, H., Glasby, G. P., Yang, Q.H., Yin, X.J., Li, J.W., and Chen, Z.Q. (2012) Formation of Fe-Mn-Si oxide and nontronite deposits in hydrothermal fields on the Valu Fa Ridge, Lau Basin. *Journal of Asian Earth Sciences*, **43**, 64–76.
Taitel-Goldman, N., Ezersky, V., and Mogilyanski, D. (2009) High-resolution transmission electron microscopy study of Fe-Mn oxides in the hydrothermal sediments of the Red Sea Deeps System. *Clays and Clay Minerals*, **57**, 465–475.
Tang, J.A. and Valix, M. (2006) Leaching of low grade limonite and nontronite ores by fungi metabolic acids. *Minerals Engineering*, **19**, 1274–1279.
Tang, W.F. (2000) *The Composition and Surface Chemical Characteristics of Fe-Mn Nodules of Several Soils in China*. PhD thesis, Huazhong Agricultural University, China, pp. 22–30
Tripathi, J.K. and Rajamani, V. (2007) Geochemistry and origin of ferruginous nodules in weathered granodioritic gneisses, Mysore Plateau, Southern India. *Geochimica et Cosmochimica Acta*, **71**, 1674–1688.
Tsubouchi, N., Mochizuki, Y., Byambajav, E., Takahashi, S., Hanaoka, Y., and Ohtsuka, Y. (2017) Catalytic performance of limonite ores in the decomposition of model compounds of biomass-derived tar. *Energy & Fuels*, **31**, 3893–3904.
Vaasjoki, M. (1985) The teutonic bore deposit, Western Australia: A lead isotope study of an ore and its gossan. *Mineralium Deposita*, **20**, 266–270.
Velasco, F., Herrero, J.M., Suárez, S., Yusta, I., Alvaro, A., and Tornos, F. (2013) Supergene features and evolution of gossans capping massive sulphide deposits in the Iberian Pyrite Belt. *Ore Geology Reviews*, **53**, 181–203.
Wang, X.M., Zhu, M.Q., Lan, S., Ginder-Vogel, M., Liu, F., and Feng, X.H. (2015) Formation and secondary mineralization of ferrihydrite in the presence of silicate and Mn(II). *Chemical Geology*, **415**, 37–46.
Williams, D., Suchowerska, A., and Airey, D. (2012) Limonite – a weathered residual soil heterogeneous at all scales. *Geotechnique Letters*, **2**, 119–122.
Wu, F., Cao, Z., Wang, S., and Zhong, H. (2017) Phase transformation of iron in limonite ore by microwave roasting with addition of alkali lignin and its effects on magnetic separation. *Journal of Alloys and Compounds*, **722**, 651–661.
Xu, W., Ding, X.G., Wu, L.B., Wang, K.Y., and Ding, N. (2011) Metallogenic features and ore prospecting potential at the north rim of the Tongling uplift, Anhui. *Geology of Anhui*, **21**, 138–142 (in Chinese).
Yao, Z.Y., Li, Y., He, J.R., and Sun, N.G. (1992) On study of ore material composition and gold occurrence of gossan-type gold deposits from Mid-Lower Reaches of Yangtze River. *Volcanology and Mineral Resource*, **13**, 59–72 (in Chinese).
Yesares, L., Sáez, R., Sel, G.R.D.L., Nieto, J.M., Aiglsperger, T., Proenza, J.A., Domínguez, C.G., and Escobar, J.M. (2015) Gold behavior in supergene profiles under changing redox conditions: the example of the Las Cruces deposit, Iberian pyrite belt. *Economic Geology*, **110**, 2109–2126.
Yesares, L., Sáez, R., Almodóvar, G.R.D., Nieto, J.M., Gómez, C., and Ovejero, G. (2017) Mineralogical evolution of the Las Cruces gossan cap (Iberian Pyrite Belt): from subaerial to underground conditions. *Ore Geology Reviews*, **80**, 377–405.
Zhao, X.Y., Ren, J., Cao, J.P., Wei, F., Zhu, C., and Fan, X., *et al*. (2017) Catalytic reforming of volatiles from biomass pyrolysis for hydrogen-rich gas production over limonite ore. *Energy & Fuels*, **31**, 4054–3060.
Zhao, Y.M., Tan, H.J., Xu, Z.N., Yuan, R.G., Bi, C.S., Zheng, R.L., Li, D.X., and Sun, J.H. (1983) *The Calcic-Skarn Iron Ore Deposits of Makeng Type in Southwestern Fujian*. Institute of Mineral Deposits, Chinese Academy of Geological Sciences, pp. 40–46.
Zhao, Y.M., Lin, W.W., Bi, C.S., Li, D.X., and Jiang, C.J. (1990) *Skarn Deposits of China*. Geological Publishing House, Beijing, China, pp. 68–75.

(*Received 8 September 2017; revised 22 May 2018; Ms. 1201; AE: H. He*)